

Rothamsted Repository Download

A - Papers appearing in refereed journals

Zhang, Y., Yang, Z., Wang, F. and Zhang, X. 2021. Comparison of soil tortuosity calculated by different methods. *Geoderma*. 402, p. 115358.
<https://doi.org/10.1016/j.geoderma.2021.115358>

The publisher's version can be accessed at:

- <https://doi.org/10.1016/j.geoderma.2021.115358>
- <https://www.sciencedirect.com/science/article/abs/pii/S0016706121004389?via%3Dihub>

The output can be accessed at:

<https://repository.rothamsted.ac.uk/item/9862v/comparison-of-soil-tortuosity-calculated-by-different-methods>.

© 29 July 2021, Please contact library@rothamsted.ac.uk for copyright queries.

1
2
3
4
5
6
7
8
9
10
11
12
13
14
15
16
17
18
19
20
21
22
23
24
25
26
27
28
29
30
31
32
33
34
35
36

Comparison of soil tortuosity calculated by different methods

Yuming Zhang¹, Zhenjun Yang², Feng Wang³, Xiaoxian Zhang^{3,4}

¹ Institute for Future Transport and Cities, Coventry University, Coventry, CV1 5FB, UK.

² Key Laboratory of Geotechnical and Structural Engineering Safety in Hubei Province, School of Civil Engineering, Wuhan University, Wuhan 430000, Hubei, China.

³ Farmland Irrigation Research Institute, Chinese Academy of Agricultural Sciences, Xinxiang 453003, Henan Province, China.

⁴ Department of Sustainable Agricultural Sciences, Rothamsted Research, Harpenden, AL5 2JQ, UK.

Abstract

Tortuosity is a parameter characterising the complexity of pore geometry in porous media for fluids and solutes to move through. It is loosely defined and has been calculated by different methods based on either the pore geometry or a special transport process. While it has been known that tortuosities calculated from different methods vary, it remains obscure if there is a one-to-one relationship between them, especially for soils which are not randomly structured but self-organised by a myriad of interactive biotic and abiotic processes. We studied this based on X-ray images of 30 soil aggregates taken from fields which have been under different land managements for more than 70 years and thus have contrasting structures. The tortuosity of every soil sample was calculated using three methods: viscous fluid flow, solute diffusion, and geometric structure of the pores, with the former two calculated from pore-scale simulations. The results showed that although the tortuosities calculated by all methods are correlated, their correlation is weak and there is no one-to-one relationship between them. On average, the tortuosity calculated from fluid flow is the highest and the geometrical tortuosity is the least, with that calculated from solute diffusion in between. The tortuosity calculated from all three methods decreases as porosity increases, but the coefficient of determination is low. We also found that the bulk diffusion coefficient cannot be predicted using geometrical tortuosity and porosity of the soil from the formulae suggested in the literature. These findings reveal that tortuosity is a process-dependent parameter rather than an intrinsic soil property, and that tortuosity calculated from different methods cannot be used interchangeably to estimate soil transport parameters.

Keywords: Tortuosity; solute diffusion; viscous fluid flow; soil aggregates; pore-scale simulation.

37 **1. Introduction**

38 Imaging technologies have been used increasingly over the past two decades to
39 investigate soil structural change following long-term and short-term agronomic practice
40 changes (Dal Ferro et al., 2013; Garbout et al., 2013; Gao et al., 2017; Bacq-Labreuil et al.,
41 2018; Galdos et al., 2019). The analysis of soil images is usually based on their
42 morphologies using parameters such as pore-size distribution, critical pore diameter,
43 Eulerian numbers and tortuosity (Rabot et al., 2018; Bacq-Labreuil et al., 2019; Koestel and
44 Schluter, 2019; Bacq-Labreuil et al., 2020; Koestel et al., 2020). Unlike other morphological
45 parameters which are scalar, tortuosity characterises how tortuous the pore geometry in a
46 soil is for fluids and solutes to move through and is hence direction-dependent (Barrande et
47 al., 2007). Although the physical meaning of the tortuosity can be adequately defined for
48 idealized media such as capillary tubes, its definition and calculation for complicated
49 materials such as soil are not trivial and continue to attract interest (Ghanbarian et al., 2013;
50 Fu et al., 2021). In the literature, the tortuosity has been calculated either as a geometrical
51 parameter, or from a specific transport process such as viscous fluid flow (Koponen et al.,
52 1996) and solute diffusion (Pisani, 2011).

53 The tortuosity of porous materials has been known to vary with its calculation method
54 (Shanti et al., 2014), and even for the same transport process, there are different ways to
55 calculate its associated tortuosity and the consequent results vary (Koponen et al., 1996;
56 Shanti et al., 2014). Despite these, it appears to have been accepted that tortuosities
57 calculated from different methods could be used interchangeably. For example, tortuosity
58 calculated from solute diffusion has been used to approximate the tortuosity of viscous fluid
59 flow (Peng et al., 2014; Backeberg et al., 2017), and the bulk diffusion coefficient of solute in
60 porous materials was estimated based on their porosity and geometrical tortuosity (Epstein,
61 1989).

62 The tortuosity of a medium for fluid flow is normally defined as the ratio between the
63 Eulerian distance between the two ends of streamlines to the average length of the
64 streamlines. In contrast, the tortuosity for solute diffusion is often calculated as the ratio of its

65 molecular diffusion coefficient to its bulk diffusion coefficient, despite the fact that, similar to
66 fluid flow, solute also moves along diffusing-lines perpendicular to the concentration
67 gradient. As there is no consensus on how to define the tortuosity for solute diffusion, its
68 calculation varies with some defining it as $\tau = \varepsilon D_0 / D_e$ (Barrande et al., 2007), while others
69 calculating it as $\tau = \varepsilon \sqrt{D_0 / D_e}$ (Epstein, 1989), where ε is porosity, D_e and D_0 are bulk diffusion
70 coefficient and molecular diffusion coefficient of a solute respectively. Inversely, these
71 formulae have also been used to estimate bulk diffusion coefficient of soils for solute to
72 move when porosity and geometrical tortuosity of the soils are known.

73 Tortuosity is a parameter characterising the impact of pore geometry of soil for fluids
74 and solutes to flow through, and it hence depends on both soil structure and the transport
75 processes. Tomography can **provide an image of soil structure** in great detail with the pixel
76 size less than micrometre (Bacq-Labreuil et al., 2018; Zhang et al., 2021), but it is unable to
77 **allow visualising fluid flow** and tracer movement through the soil. Pore-scale simulations can
78 bridge this gap (Zhang et al., 2016a; Zhang et al., 2016b), enabling us to mimic viscous fluid
79 flow and solute diffusion in the pore space. It has been used in combination with imaging
80 technology to calculate tortuosity of both viscous flow and molecular diffusion in granular
81 materials (Matyka et al., 2008; Shanti et al., 2014; Fu et al., 2021). However, soils are
82 different as their structure is not purely random but highly self-organised, mediated by a
83 multitude of interactive biotic and abiotic processes, especially microbial activity and
84 decomposition of soil organic matter (Young and Crawford, 2004; Crawford et al., 2012;
85 Rabbi et al., 2020).

86 The purpose of this paper is to investigate how soil tortuosities calculated from different
87 methods differ from each other, and if there is a generic relationship between them which
88 applies to all soils regardless of their structures. We compared three methods; the first two
89 **were** for fluid flow and solute diffusion, with their associated tortuosity calculated from pore-
90 scale simulations; the third one was geometrical, calculated based on how pores were
91 connected spatially. We analysed 30 soil aggregates with contrasting structures; they were

92 taken from fields under different land managements for more than 70 years. Considering that
93 one important application of the tortuosity is to estimate soil transport parameters, we took
94 bulk diffusion coefficient as an example, examining if the geometrical tortuosity and porosity
95 can be used to reliably estimate the average ability of soils to transport solutes.

96 **2. Materials and methods**

97 **2.1. The soils**

98 The soils used in this work were **those studied previously** (Bacq-Labreuil et al., 2018).
99 They were sampled from a long-term experiment established in 1945 at Rothamsted
100 Research in the UK to test the impact of different land managements on carbon dynamics
101 and ecological yield. Details of the experiment **were** given in the literature (Gregory et al.,
102 2016; Hirsch et al., 2017; Bacq-Labreuil et al., 2018). **The soil is Chromic Luvisol, having a**
103 **silty clay loam texture developed on recent clay-with-flints over Eocene London Clay**
104 **(Gregory et al., 2016). Before the management change in 1945, the weight-fraction of sand,**
105 **silt and clay in the soil was 15%, 59% and 26% respectively. Overall,** 12 aggregates were
106 taken from an arable land, 11 from a permanent grassland, and 9 from a fallow plot. Each
107 aggregate was scanned using X-ray Computed Tomography at resolution of 1.5 μ m, and the
108 size of each image used in the following analysis was 650x480x400 voxels (Bacq-Labreuil et
109 al., 2018).

110 **2.2. Pore-scale simulation**

111 We calculated the tortuosity associated with fluid flow and solute diffusion as these are
112 the two most important transport processes in terrestrial systems, controlling all soil
113 functions including biogeochemical reactions and root uptake of water and nutrients. The
114 tortuosity for each transport process was calculated based on pore-scale simulations using
115 the Lattice Boltzmann model we developed previously (Zhang et al., 2016a; Li et al., 2018b).
116 For completeness, we briefly explain the method and, importantly, how it was used to
117 calculate the tortuosity.

118 **2.2.1. Viscous fluid flow**

119 Viscous fluid flow through the pore space of the soils was simulated using the following
 120 multiple-relaxation time Lattice Boltzmann model (d'Humières et al., 2002)

$$121 \quad f_i(\mathbf{x} + \delta t \mathbf{e}_i, t + \delta t) = f_i(\mathbf{x}, t) + M^{-1} S M \left[f_i^{eq}(\mathbf{x}, t) - f_i(\mathbf{x}, t) \right], \quad (1)$$

122 where $f_i(\mathbf{x}, t)$ is the distribution function at location \mathbf{x} and time t moving with lattice velocity \mathbf{e}_i ,

123 δx is the voxel size, δt is the time step, $f_i^{eq}(\mathbf{x}, t)$ is the equilibrium distribution function, M is

124 a transform matrix and S is the collision matrix. The transformation matrix M converts the

125 distribution functions into a moment space prior to performing the collision operation -

126 $m = S M \left[f_i^{eq}(\mathbf{x}, t) - f_i(\mathbf{x}, t) \right]$. The post-collision results were then transformed back to

127 distribution functions by $M^{-1} m$. We used the D3Q19 lattice model in which the distribution

128 functions move in 19 direction with lattice velocities $(0, 0, 0)$, $(\pm \delta x / \delta t, \pm \delta x / \delta t, 0)$,

129 $(0, \pm \delta x / \delta t, \pm \delta x / \delta t)$, $(\pm \delta x / \delta t, 0, \pm \delta x / \delta t)$ and $(\pm \delta x / \delta t, \pm \delta x / \delta t, \pm \delta x / \delta t)$ (Qian et al.,

130 1992). Detail of the transform matrix was given in the literature (d'Humières et al., 2002).

131 The collision operation is described by the following diagonal matrix (Pan et al., 2006):

$$132 \quad S = (s_0, s_1, s_2, s_3, s_4, s_5, s_6, s_7, s_8, s_9, s_{10}, s_{11}, s_{12}, s_{13}, s_{14}, s_{15}, s_{16}, s_{17}, s_{18})^T, \\
 s_0 = s_3 = s_5 = s_7 = 0, \\
 s_1 = s_2 = s_{9-15} = 1 / \tau, \\
 s_4 = s_6 = s_8 = s_{16-18} = 8(2 - \tau^{-1}) / (8 - \tau^{-1}). \quad (2)$$

133 The equilibrium distribution functions used in the simulations are

$$134 \quad f_i^{eq} = w_i \left[\rho + \rho_0 \left(\frac{3 \mathbf{e}_i \cdot \mathbf{u}}{c^2} + \frac{9 (\mathbf{e}_i \cdot \mathbf{u})^2}{2c^4} - \frac{3 \mathbf{u} \cdot \mathbf{u}}{2c^2} \right) \right], \quad (3) \\
 w_0 = 1/3, \\
 w_i = 1/18, \quad \|\mathbf{e}_i\| = \delta x / \delta t \\
 w_i = 1/36 \quad \|\mathbf{e}_i\| = \sqrt{2} \delta x / \delta t$$

135 where $c = \delta x / \delta t$ and ρ_0 is a reference fluid density to ensure fluid incompressibility when

136 flow is in steady state (Zou et al., 1995). Bulk fluid density ρ and velocity \mathbf{u} during the

137 simulation were updated by

$$\begin{aligned} \rho &= \sum_{i=0}^{18} f_i, \\ \rho_0 \mathbf{u} &= \sum_{i=1}^{18} f_i \mathbf{e}_i. \end{aligned} \quad (4)$$

139 The kinematic fluid viscosity μ and the fluid pressure p simulated by the Lattice Boltzmann
 140 method are $\mu = \delta x^2 (\tau - 0.5) / 6 \delta t$ and $p = \rho \delta x^2 / 3 \delta t^2$ respectively. Advancing one time step
 141 needs two calculations; the first one is collision: $f_i^* = f_i(\mathbf{x}, t) + M^{-1} SM [f_i^{eq}(\mathbf{x}, t) - f_i(\mathbf{x}, t)]$, and
 142 the second one is to move the post-collision result f_i^* at location \mathbf{x} to $\mathbf{x} + \delta t \mathbf{e}_i$ during the time
 143 period of δt . Whenever a particle hits a solid voxel during its movement following the
 144 collision, it is bounced back to its original location to make the walls of the solid voxels a
 145 non-slip boundary where the fluid velocity is zero.

146 In all simulations, the initial fluid velocity was zero everywhere and the flow was
 147 initialized by a pressure gradient generated by imposing a constant pressure on one face of
 148 the image and a low pressure on its opposite face. The flow was simulated to steady state –
 149 deemed to have reached when the relative difference between the sum of the absolute fluid
 150 velocity at all voxels at two time points separated by 300 time-steps was less than 10^{-6} .
 151 When fluid was at steady state, its associated tortuosity in the direction along which the
 152 pressure gradient was generated was calculated from (Koponen et al., 1996; Duda et al.,
 153 2011):

$$\tau_f = \frac{\sum_{i=1}^N \|\mathbf{u}(\mathbf{x}_i)\|}{\sum_{i=1}^N u_l(\mathbf{x}_i)}, \quad (5)$$

155 where N is the number of fluid voxels, $u_l(\mathbf{x}_i)$ is the velocity component at the voxel centred
 156 at \mathbf{x}_i and in the l direction aligning with the pressure gradient.

157 2.2.2. Diffusive solute transport

158 Solute diffusion in the pore space was also simulated using the Lattice Boltzmann model
 159 as follows assuming the water was stagnant (Zhang et al., 2016a):

$$g_i(\mathbf{x} + \delta t \mathbf{e}_i, t + \delta t) = g_i(\mathbf{x}, t) + \lambda [g_i^{eq}(\mathbf{x}, t) - g_i(\mathbf{x}, t)], \quad (6)$$

161 where $g_i(\mathbf{x}, t)$ is solute particle distribution function at location \mathbf{x} and time t moving with lattice
162 velocity \mathbf{e}_i , $g_i^{eq}(\mathbf{x}, t)$ is the associated equilibrium distribution function, and λ is a relaxation
163 parameter. Unlike viscous fluid flow, solute diffusion is constrained by mass conservation
164 only and we thus reduced the lattice velocities from 19 to 7: $(0, 0, 0)$, $(\pm\delta x/\delta t, 0, 0)$,
165 $(0, \pm\delta x/\delta t, 0)$ and $(0, 0, \pm\delta x/\delta t)$. The associated equilibrium distribution functions for the
166 seven lattice velocities were the same: $g_i^{eq}(\mathbf{x}, t) = c(\mathbf{x}, t)/7$, where $c(\mathbf{x}, t)$ is solute
167 concentration at location \mathbf{x} and time t . During the simulation, the concentration c and
168 diffusive flux \mathbf{J} were updated from (Zhang et al., 2010)

$$169 \quad \begin{aligned} c(\mathbf{x}, t) &= \sum_{i=0}^6 g_i(\mathbf{x}, t), \\ \mathbf{J}(\mathbf{x}, t) &= (1.0 - 0.5\lambda) \sum_{i=1}^6 \mathbf{e}_i g_i(\mathbf{x}, t). \end{aligned} \quad (7)$$

170 The diffusion coefficient simulated by the model above is $D = \delta x^2(1/\lambda - 0.5)/3.5\delta t$. Similar as
171 for viscous flow, simulating solute diffusion also needs two calculations to advance one time
172 step: a collision calculation: $g_i^* = g_i(\mathbf{x}, t) + \lambda[g_i^{eq}(\mathbf{x}, t) - g_i(\mathbf{x}, t)]$, and a streaming calculation
173 to move g_i^* from \mathbf{x} to $\mathbf{x} + \delta t \mathbf{e}_i$ during the time period of δt . If g_i^* hits a solid wall during its
174 movement, it is bounced back to where it came from to make the wall impermeable to the
175 solute.

176 Similar as in the fluid flow simulation, the initial concentration in the solute simulation
177 was also zero everywhere and solute movement was initiated by a concentration gradient
178 generated by imposing a constant concentration at one face of the sample and a low
179 concentration on its opposite face. The diffusion was simulated to steady state - deemed to
180 have reached once the relative difference between the sum of the absolute diffusive flux in
181 all voxels at two time points separated by 300 time-steps was less than 10^{-6} . At steady state,
182 the diffusive fluxes at all voxels were sampled to calculate the tortuosity in a similar way as
183 in the fluid flow:

184
$$\tau_d = \frac{\sum_{i=1}^N \|J(x_i)\|}{\sum_{i=1}^N J_l(x_i)} \quad (8)$$

185 where $J(x_i)$ is the diffusive flux vector at voxel centred at x_i and $J_l(x_i)$ is its associated
 186 component in the l direction in parallel with the concentration gradient generated across the
 187 sample.

188 When the diffusion was at steady state, we also calculated the bulk diffusion coefficient
 189 D_e for each sample as follows:

190
$$D_e = \frac{L \sum_{i=1}^N J_l(x_i)}{N(C_1 - C_0)}, \quad (9)$$

191 where L is the length of the soil sample in the direction where the concentration gradient was
 192 generated, and C_1 and C_0 are the high and low concentrations imposed on the two opposite
 193 faces of the sample, respectively, other variables are the same as those in Eqs. (5) and (8).

194 When soil is anisotropic, the tortuosity calculated using the method above varies with
 195 direction. To examine soil anisotropy, for each sample we calculated its tortuosity in different
 196 directions by switching the pressure and concentration gradients between the three
 197 orthogonal directions.

198 **2.2.3. Geometrical tortuosity**

199 We calculated the geometric tortuosity of each soil sample based on its pore geometry.
 200 Different methods are available to calculate geometrical tortuosity and in this paper we used
 201 a plugin in Image J developed by Roque and Costa (2020); it was based on the geodesic
 202 reconstruction method (Gommes et al., 2009), with the tortuosity calculated as the ratio
 203 between the geodesic distance and the Eulerian distance between two parallel planes.

204 **3. Results**

205 Figure 1 shows the pore geometry of three aggregates with each representing one
 206 treatment. Since we aimed to compare tortuosities calculated from different methods rather
 207 than to discuss how intra-aggregate structure and its associated tortuosity changed in

208 response to the land management changes taking place 70 years ago, we pooled all results
209 except where otherwise stated in the following analysis.

210 **3.1. Tortuosity**

211 The tortuosity calculated from the three methods for most aggregates was in the range
212 of 1.2 - 2.0, depending on aggregate and the calculation method. The tortuosity of the same
213 sample varied with the method used to calculate it. Figure 2A compares the [transport](#)
214 [tortuosity](#) calculated from solute diffusion and the geometrical tortuosity for all 30 samples in
215 the three directions. On average, they are positively correlated, but there is no one-to-one
216 relationship between them and the correlation is weak. Overall, the [transport tortuosity](#) (the
217 horizontal axis) is higher than the geometrical tortuosity with the majority of the results falling
218 below the 1:1 line. The deviation from the 1:1 line widens as the tortuosity increases.

219 Figure 2B compares the [transport tortuosity](#) and the [flow tortuosity](#) calculated from fluid
220 flow for all 30 samples in the three directions. On average, the [flow tortuosity](#) (the horizontal
221 axis) is higher than the [transport tortuosity](#) with most results falling below the 1:1 line. Similar
222 to Figure 2A, the deviation between them also increases as the tortuosity increases.

223 **3.2. Porosity-tortuosity relationship**

224 Figure 3 shows the change in tortuosity with porosity for all samples taken from each
225 treatment. Regardless of the calculation method, the tortuosity is positively correlated with
226 the porosity, but their correlation is weak. Empirical formulae including power-law function
227 and exponential function have been used to fit the porosity-tortuosity relationship (Matyka et
228 al., 2008), and we fitted the results to a power-law function. The accuracy of the fitting varies
229 between the calculation method, with the coefficient of determination increasing from 0.27
230 for the [flow tortuosity](#) to 0.67 for the geometrical tortuosity and the exponent varying between
231 -0.277 and - 0.196. All aggregates are cuboid and the results showed that the geometrical
232 tortuosity and the [transport tortuosity](#) in the x direction (shown in Figure 1) were slightly
233 higher than that in other two directions. In contrast, the [flow tortuosity](#) was almost the same
234 in all three directions.

235 **4. Discussion**

236 4.1. Tortuosity calculated by different methods

237 Tortuosity is a parameter characterising how the pore geometry in a soil modulates fluid
238 flow and solute transport. Although the physical meaning of the tortuosity can be accurately
239 defined and calculated for idealised media such as capillary tubes, their extrapolation to soils
240 is not trivial and continues to be a research interest (Ghanbarian et al., 2013; Lala, 2020; Fu
241 et al., 2021). One important question is to what extent tortuosities calculated from different
242 methods are interchangeable. This is practically attractive as soil porosity and geometrical
243 tortuosity are relatively easy to measure and calculate, and if there is a one-to-one
244 correlation between tortuosities associated with different transport processes, these easy-to-
245 measure geometrical parameters can be used to estimate transport parameters which are
246 far more complicated to measure and calculate. Early theoretical analysis indicated that bulk
247 diffusion coefficient and permeability of porous medium were related to its geometrical
248 tortuosity and porosity (Epstein, 1989), and there appears to be a consensus that knowing
249 geometrical tortuosity and porosity of a soil would be sufficient to calculate its transport
250 parameters associated with different transport processes (Shanti et al., 2014). An typical
251 example is solute diffusion, where analytical formulae had been developed to calculate its
252 bulk diffusion coefficient in soils using their geometrical tortuosity and porosity (Shanti et al.,
253 2014; Fu et al., 2021). These analytical formulae, however, were derived based on capillary
254 tubes or granular media, and it remains elusive if they apply to soils which are not randomly
255 packed particles but self-organized porous assemblage formed by a multitude of interactive
256 biotic and abiotic processes operating across a wide range of scales (Young and Crawford,
257 2004; Crawford et al., 2012). The results calculated from the 30 soil aggregates with
258 contrasting structures indicated that these formulae do not apply, and that the tortuosities
259 calculated from different methods are only loosely correlated (Figure 3). In particular, the
260 flow tortuosity is the highest and the geometrical tortuosity is the least, with the transport
261 tortuosity in between. This is anticipated as fluid flow is viscous and the non-slip nature of
262 pore walls means that fluid flows preferentially into large pores bypassing small pores. As a
263 result, spatially connected large pores affect viscous flow and its associated tortuosity more

264 than small pores (Zhang et al., 2021). In contrast, **solute can slip over pore walls and the**
265 **diffusive flux is hence not predominantly controlled by large pores.** For example, the
266 permeability of a cylindrical pore for viscous fluid flow is proportional to the square of its
267 diameter, while its bulk diffusion coefficient for solute transport is independent of the pore
268 diameter.

269 Similar to fluids in soil which flow along streamlines, solute diffusion also follows
270 streamline-like pathways which are perpendicular to the concentration gradient. In lieu of
271 using bulk diffusion coefficient to estimate the **transport tortuosity**, we directly calculated it
272 based on the diffusive flux in all voxels calculated from the pore-scale simulation, which is
273 more physically sound. While the resistance of small pores to solute diffusion is not as
274 significant as to viscous fluid flow, connected large pores are still easy for solute to move
275 through. Therefore, although the **transport tortuosity** is smaller than the **flow tortuosity**, with
276 few exceptions, it is still greater than the geometrical tortuosity (Figure 2).

277 For soil taken from each of the three treatments, its tortuosity calculated by different
278 methods decreases as its **porosity increases**, but the coefficient of determination is low,
279 especially for the **flow tortuosity**. This was expected as tortuosity associated with a transport
280 or flow process in a soil depends not only on how many pores are in the soil but also on how
281 pores of different sizes are connected spatially; this applies to the geometrical tortuosity
282 which also depends on pore connection. The variation in tortuosity with porosity for soil
283 taken from each of the three treatments can be fitted to a power-law function with its
284 exponent varying from -0.277 to -0.196, depending on the calculation method (Figure 3).
285 This is less than those reported in the literature, which, for example, is - 0.5 for rock (Lala,
286 2020), indicating that the tortuosity of soils is less sensitive to porosity change due to their
287 self-organized structures (Young and Crawford, 2004; Crawford et al., 2012).

288 Soil is hierarchically structured, formed by interactive abiotic and abiotic processes
289 (Young and Crawford, 2004). It contains a large number of large pore bodies, which
290 contribute to porosity but have limited impact on transport ability. For a hydraulic conduit
291 consisting of a series of pores, it is the small pores that control fluid flow – the so-called

292 bottleneck - as average permeability of the conduit is the geometric mean of the permeability
293 of all pores (Li et al., 2018a). As an illustration, Figure 4 shows how the pores of different
294 sizes are connected spatially in a soil sample. It is evident that there are a number of large
295 pore bodies linked by small pores, which make only limited contributions to the ability of the
296 soil to transport fluids and solutes.

297 **4.2. Implications**

298 The application of tomography technologies in soil research over the past decade has
299 generated massive 3D images of intact soils with different textures under various agricultural
300 managements and climatic conditions (Baveye et al., 2018). In parallel, development in
301 commercial and open-source software has made image analysis readily accessible. For
302 example, morphological parameters such as pore-size distribution, geometrical tortuosity
303 and pore skeletons in an image can be quickly calculated using the plugins in Image J
304 (Schindelin et al., 2012; Roque and Costa, 2020). The ultimate purpose of soil image
305 analysis is to link these morphological parameters to soil functions (Graczyk and Matyka,
306 2020), especially fluid flow and solute diffusion which are fundamental as they control almost
307 all physical and biogeochemical reactions and modulate root uptake of water and nutrients
308 from soils (Mooney et al., 2012; Helliwell et al., 2017; Rabbi et al., 2018).

309 Unlike morphological parameters, calculating transport parameters needs to simulate
310 transport processes which are governed by a set of nonlinear partial differential equations.
311 Solving these equations is computationally demanding because the soil samples should be
312 large enough to be representative while their voxel size needs to be small enough to capture
313 key microscopic features. Most soil images thus consist of hundreds of millions of voxels;
314 simulating any transport process in such images requires high performance computing even
315 using smart storage to remove the solid voxels which are not involved in fluid flow and solute
316 diffusion (Wang et al., 2005). Currently, most studies of soil structural alteration induced by
317 agronomic practice changes have focused on morphological parameters with a view that
318 these parameters can be used to estimate transport parameters (Epstein, 1989). One typical
319 example is the bulk diffusion coefficient of solute transport, which has been proven,

320 theoretically, related to porosity and geometrical tortuosity of soil in $D_e = D_0 \sqrt{\varepsilon/\tau^2}$ (Epstein,
321 1989). This relationship has been accepted and even used widely to calculate tortuosity from
322 pore-scale simulation (Shanti et al., 2014), and experimental measurement (He et al., 2013).
323 To examine if this formula holds for the 30 soils we studied, we compared the bulk diffusion
324 coefficient directly calculated from the pore-scale simulations with that estimated from the
325 above formula using the geometrical tortuosity and porosity of each soil sample. The results
326 were shown in Figure 5. **It is manifest** that the formula underestimated the ability of the soils
327 to transport solutes because it was derived based on idealized media which differ from soils.
328 However, we found that the bulk diffusion coefficient of the soils can be estimated by
329 modifying the formula to $D_e = kD_0 \sqrt{\varepsilon/\tau^2}$ with $k=1.52$. This is consistent with the results of Fu
330 et al (2021) who found that the “tortuosity” calculated from $\sqrt{\varepsilon D_0 / D_e}$ was substantially greater
331 than the **flow and transport tortuosity**. **We cannot verify that $k=1.52$ is a universal coefficient**
332 **or only applies to the 30 samples due to the limited number of soil samples we simulated.**
333 Nonetheless, these results suggest that great care should be taken when using porosity and
334 geometrical tortuosity of soils to predict their transport parameters for fluid flow and solute
335 diffusion.

336 **5. Conclusion**

337 We calculated the tortuosity of 30 intact soil aggregates using different methods and
338 found that the tortuosity is a process-based parameter rather than an intrinsic soil property in
339 that the tortuosity of a soil varies with the method used to calculate it. For tortuosities
340 calculated using the three methods: viscous flow, solute diffusion and pore geometry, the
341 **flow tortuosity** is the highest and the geometrical tortuosity is the least, with the transport
342 tortuosity in between. The tortuosities calculated by different methods are only weakly
343 correlated, suggesting that they cannot be used interchangeably. The tortuosity of soil taken
344 from the same treatment decreases as its porosity increases, but the coefficient of
345 determination is low. The bulk solute diffusion coefficient calculated directly from the pore-

346 scale simulation showed that it cannot be predicted using soil porosity and geometrical
347 tortuosity from the formulae suggested in the literature.

348 **Acknowledgements**

349 YMZ thanks Coventry University for offering her a PhD studentship, and ZJY receives
350 funding from the National Natural Science Foundation of China (No. 51974202, No.
351 51779222). FW acknowledges the financial support of the National Natural Science
352 Foundation of China (No. 51790535) and the Basic Scientific Research Project of Chinese
353 Academy of Agricultural Sciences (Grant No. FIRI201606). The work at Rothamsted
354 Research forms part of the soils to nutrition (S2N) strategic programme (BBS/E/C/000I0310)
355 funded by the Biotechnology and Biological Sciences Research Council (BBSRC) of the UK,
356 and the project (NE/T010487/1) funded by the Natural Environmental Research Council
357 (NERC) of the UK.

359 **References**

- 360 Backeberg, N.R., Iacoviello, F., Rittner, M., Mitchell, T.M., Jones, A.P., Day, R., Wheeler, J.,
 361 Shearing, P.R., Vermeesch, P., Striolo, A., 2017. Quantifying the anisotropy and
 362 tortuosity of permeable pathways in clay-rich mudstones using models based on X-
 363 ray tomography. *Sci Rep* 7, 12.
- 364 Bacq-Labreuil, A., Crawford, J., Mooney, S.J., Neal, A.L., Akkari, E., McAuliffe, C., Zhang,
 365 X.X., Redmile-Gordon, M., Ritz, K., 2018. Effects of cropping systems upon the
 366 three-dimensional architecture of soil systems are modulated by texture. *Geoderma*
 367 332, 73-83.
- 368 Bacq-Labreuil, A., Crawford, J., Mooney, S.J., Neal, A.L., Ritz, K., 2019. Cover crop species
 369 have contrasting influence upon soil structural genesis and microbial community
 370 phenotype. *Sci Rep* 9, 9.
- 371 Bacq-Labreuil, A., Crawford, J., Mooney, S.J., Neal, A.L., Ritz, K., 2020. Recovery of soil
 372 structure under long-term fallow in response to annual or perennial cropping requires
 373 at least 10 years after conversion. *European Journal of Soil Science* 9, 9.
- 374 Barrande, M., Bouchet, R., Denoyel, R., 2007. Tortuosity of porous particles. *Anal. Chem.*
 375 79(23), 9115-9121.
- 376 Baveye, P.C., Otten, W., Kravchenko, A., Balseiro-Romero, M., Beckers, E., Chalhoub, M.,
 377 Darnault, C., Eickhorst, T., Garnier, P., Hapca, S., Kiranyaz, S., Monga, O., Mueller,
 378 C.W., Nunan, N., Pot, V., Schluter, S., Schmidt, H., Vogel, H.J., 2018. Emergent
 379 Properties of Microbial Activity in Heterogeneous Soil Microenvironments: Different
 380 Research Approaches Are Slowly Converging, Yet Major Challenges Remain. *Front.*
 381 *Microbiol.* 9, 48.
- 382 Crawford, J.W., Deacon, L., Grinev, D., Harris, J.A., Ritz, K., Singh, B.K., Young, I., 2012.
 383 Microbial diversity affects self-organization of the soil-microbe system with
 384 consequences for function. *J. R. Soc. Interface* 9(71), 1302-1310.
- 385 d'Humières, D., Ginzburg, I., Krafczyk, M., Lallemand, P., Luo, L.S., 2002. Multiple-
 386 relaxation-time lattice Boltzmann models in three dimensions. *Philos. Trans. R. Soc.*
 387 *Lond. Ser. A-Math. Phys. Eng. Sci.* 360(1792), 437-451.
- 388 Dal Ferro, N., Charrier, P., Morari, F., 2013. Dual-scale micro-CT assessment of soil
 389 structure in a long-term fertilization experiment. *Geoderma* 204, 84-93.
- 390 Duda, A., Koza, Z., Matyka, M., 2011. Hydraulic tortuosity in arbitrary porous media flow.
 391 *Phys. Rev. E* 84(3), 8.
- 392 Epstein, N., 1989. ON TORTUOSITY AND THE TORTUOSITY FACTOR IN FLOW AND
 393 DIFFUSION THROUGH POROUS-MEDIA. *Chem. Eng. Sci.* 44(3), 777-779.
- 394 Fu, J.L., Thomas, H.R., Li, C.F., 2021. Tortuosity of porous media: Image analysis and
 395 physical simulation. *Earth-Sci. Rev.* 212, 30.
- 396 Galdos, M.V., Pires, L.F., Cooper, H.V., Calonego, J.C., Rosolem, C.A., Mooney, S.J., 2019.
 397 Assessing the long-term effects of zero-tillage on the macroporosity of Brazilian soils
 398 using X-ray Computed Tomography. *Geoderma* 337, 1126-1135.
- 399 Gao, L.L., Becker, E., Liang, G.P., Houssou, A.A., Wu, H.J., Wu, X.P., Cai, D.X., Degre, A.,
 400 2017. Effect of different tillage systems on aggregate structure and inner distribution
 401 of organic carbon. *Geoderma* 288, 97-104.
- 402 Garbout, A., Munkholm, L.J., Hansen, S.B., 2013. Temporal dynamics for soil aggregates
 403 determined using X-ray CT scanning. *Geoderma* 204, 15-22.
- 404 Ghanbarian, B., Hunt, A.G., Ewing, R.P., Sahimi, M., 2013. Tortuosity in Porous Media: A
 405 Critical Review. *Soil Sci. Soc. Am. J.* 77(5), 1461-1477.
- 406 Gommès, C.J., Bons, A.-J., Blacher, S., Dunsmuir, J.H., Tsou, A.H., 2009. Practical methods
 407 for measuring the tortuosity of porous materials from binary or gray-tone tomographic
 408 reconstructions. *AIChE Journal* 55(8), 2000-2012.
- 409 Graczyk, K.M., Matyka, M., 2020. Predicting porosity, permeability, and tortuosity of porous
 410 media from images by deep learning. *Sci Rep* 10(1), 11.

411 Gregory, A.S., Dungait, J.A.J., Watts, C.W., Bol, R., Dixon, E.R., White, R.P., Whitmore,
412 A.P., 2016. Long-term management changes topsoil and subsoil organic carbon and
413 nitrogen dynamics in a temperate agricultural system. *Eur. J. Soil Sci.* 67(4), 421-
414 430.

415 He, W.D., Zou, J., Wang, B., Vilayurganapathy, S., Zhou, M., Lin, X., Zhang, K.H.L., Lin,
416 J.H., Xu, P., Dickerson, J.H., 2013. Gas transport in porous electrodes of solid oxide
417 fuel cells: A review on diffusion and diffusivity measurement. *J. Power Sources* 237,
418 64-73.

419 Helliwell, J.R., Sturrock, C.J., Mairhofer, S., Craigon, J., Ashton, R.W., Miller, A.J., Whalley,
420 W.R., Mooney, S.J., 2017. The emergent rhizosphere: imaging the development of
421 the porous architecture at the root-soil interface. *Sci Rep* 7, 10.

422 Hirsch, P.R., Jhurrea, D., Williams, J.K., Murray, P.J., Scott, T., Misselbrook, T.H.,
423 Goulding, K.W.T., Clark, I.M., 2017. Soil resilience and recovery: rapid community
424 responses to management changes. *Plant Soil* 412(1-2), 283-297.

425 Koestel, J., Larsbo, M., Jarvis, N., 2020. Scale and REV analyses for porosity and pore
426 connectivity measures in undisturbed soil. *Geoderma* 366, 114206.

427 Koestel, J., Schluter, S., 2019. Quantification of the structure evolution in a garden soil over
428 the course of two years. *Geoderma* 338, 597-609.

429 Koponen, A., Kataja, M., Timonen, J., 1996. Tortuous flow in porous media. *Phys. Rev. E*
430 54(1), 406-410.

431 Lala, A.M.S., 2020. A novel model for reservoir rock tortuosity estimation. *J. Pet. Sci. Eng.*
432 192, 7.

433 Li, Z.Y., Wang, D., Zhang, X.X., Crawford, J.W., 2018a. Water flow across the interface of
434 contrasting materials: Pressure discontinuity and its implications. *J. Hydrol.* 566, 435-
435 440.

436 Li, Z.Y., Zhang, X.X., Wang, D., Liu, Y., 2018b. Direct methods to calculate the mass
437 exchange between solutes inside and outside aggregates in macroscopic model for
438 solute transport in aggregated soil. *Geoderma* 320, 126-135.

439 Matyka, M., Khalili, A., Koza, Z., 2008. Tortuosity-porosity relation in porous media flow.
440 *Phys. Rev. E* 78(2), 8.

441 Mooney, S.J., Pridmore, T.P., Helliwell, J., Bennett, M.J., 2012. Developing X-ray Computed
442 Tomography to non-invasively image 3-D root systems architecture in soil. *Plant Soil*
443 352(1-2), 1-22.

444 Pan, C.X., Luo, L.S., Miller, C.T., 2006. An evaluation of lattice Boltzmann schemes for
445 porous medium flow simulation. *Computers & Fluids* 35(8-9), 898-909.

446 Peng, S., Marone, F., Dultz, S., 2014. Resolution effect in X-ray microcomputed tomography
447 imaging and small pore's contribution to permeability for a Berea sandstone. *J.*
448 *Hydrol.* 510, 403-411.

449 Pisani, L., 2011. Simple Expression for the Tortuosity of Porous Media. *Transp. Porous*
450 *Media* 88(2), 193-203.

451 Qian, Y.H., Dhumieres, D., Lallemand, P., 1992. Lattice BGK models for Navier-Stokes
452 equation. *Europhysics Letters* 17(6BIS), 479-484.

453 Rabbi, S.M.F., Minasny, B., McBratney, A.B., Young, L.M., 2020. Microbial processing of
454 organic matter drives stability and pore geometry of soil aggregates. *Geoderma* 360,
455 4.

456 Rabbi, S.M.F., Tighe, M.K., Flavel, R.J., Kaiser, B.N., Guppy, C.N., Zhang, X.X., Young,
457 I.M., 2018. Plant roots redesign the rhizosphere to alter the three-dimensional
458 physical architecture and water dynamics. *New Phytol.* 219(2), 542-550.

459 Rabot, E., Wiesmeier, M., Schluter, S., Vogel, H.J., 2018. Soil structure as an indicator of
460 soil functions: A review. *Geoderma* 314, 122-137.

461 Roque, W.L., Costa, R.R.A., 2020. A plugin for computing the pore/grain network tortuosity
462 of a porous medium from 2D/3D MicroCT image. *Applied Computing and*
463 *Geosciences* 5, 100019.

464 Schindelin, J., Arganda-Carreras, I., Frise, E., Kaynig, V., Longair, M., Pietzsch, T.,
465 Preibisch, S., Rueden, C., Saalfeld, S., Schmid, B., Tinevez, J.Y., White, D.J.,

466 Hartenstein, V., Eliceiri, K., Tomancak, P., Cardona, A., 2012. Fiji: an open-source
467 platform for biological-image analysis. *Nat. Methods* 9(7), 676-682.

468 Shanti, N.O., Chan, V.W.L., Stock, S.R., De Carlo, F., Thornton, K., Faber, K.T., 2014. X-ray
469 micro-computed tomography and tortuosity calculations of percolating pore networks.
470 *Acta Mater.* 71, 126-135.

471 Wang, J.Y., Zhang, X.X., Bengough, A.G., Crawford, J.W., 2005. Domain-decomposition
472 method for parallel lattice Boltzmann simulation of incompressible flow in porous
473 media. *Phys. Rev. E* 72(1), 11.

474 Young, I.M., Crawford, J.W., 2004. Interactions and self-organization in the soil-microbe
475 complex. *Science* 304(5677), 1634-1637.

476 Zhang, X., Crawford, J.W., Flavel, R.J., Young, I.M., 2016a. A multi-scale Lattice Boltzmann
477 model for simulating solute transport in 3D X-ray micro-tomography images of
478 aggregated porous materials. *J. Hydrol.* 541, Part B, 1020-1029.

479 Zhang, X., Neal, A.L., Crawford, J.W., Bacq-Labreuil, A., Akkari, E., Rickard, W., 2021. The
480 effects of long-term fertilizations on soil hydraulic properties vary with scales. *J.*
481 *Hydrol.* 593, 125890.

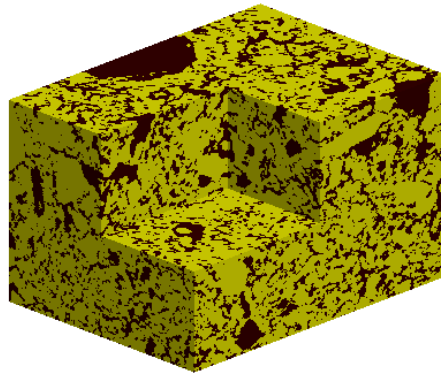
482 Zhang, X.X., Crawford, J.W., Young, I.M., 2016b. A Lattice Boltzmann model for simulating
483 water flow at pore scale in unsaturated soils. *J. Hydrol.* 538, 152-160.

484 Zhang, X.X., Qi, X.B., Qiao, D.M., 2010. Change in macroscopic concentration at the
485 interface between different materials: Continuous or discontinuous. *Water Resour.*
486 *Res.* 46, 12.

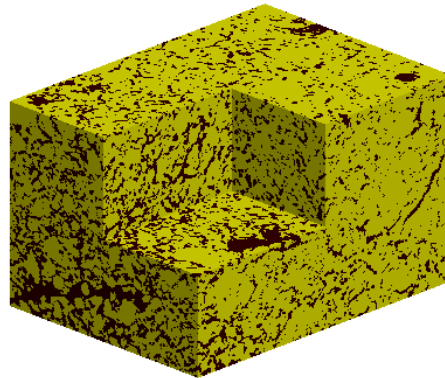
487 Zou, Q.S., Hou, S.L., Chen, S.Y., Doolen, G.D., 1995. An improved incompressible Lattice
488 Boltzmann model for time-independent flows. *Journal of Statistical Physics* 81(1-2),
489 35-48.

490

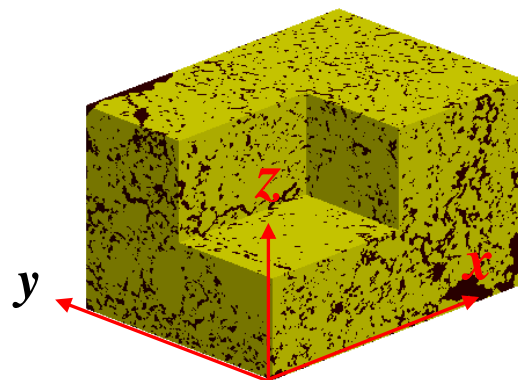
491



492
493

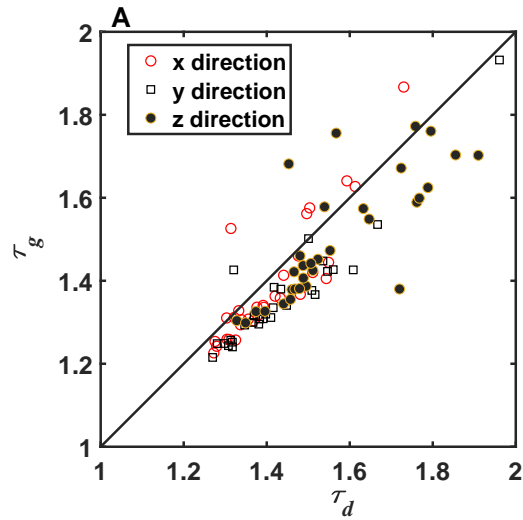


494
495

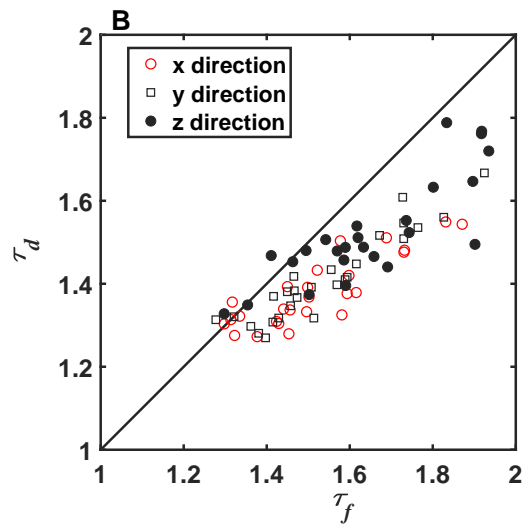


496
497
498
499
500
501

Figure 1. Three soil images with each representing illustratively the impact of land management. (A) grassland, (B) arable land, (C) bare fallow land.



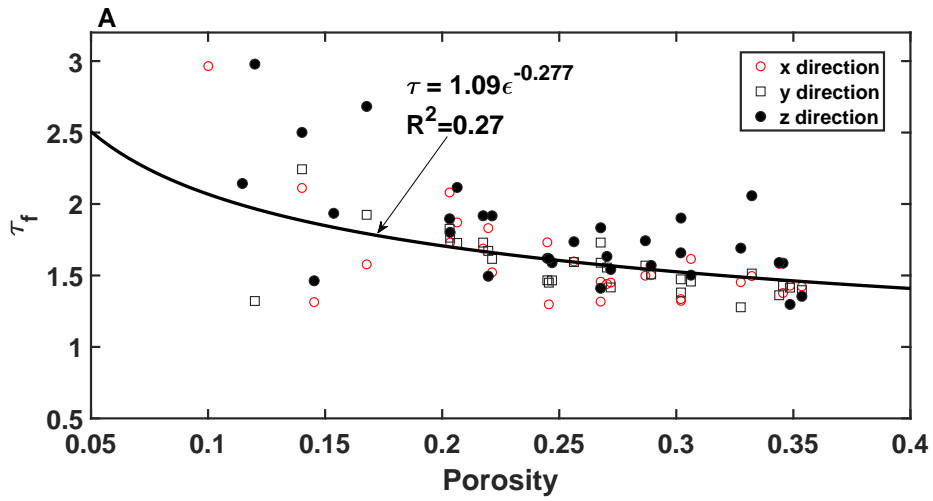
502



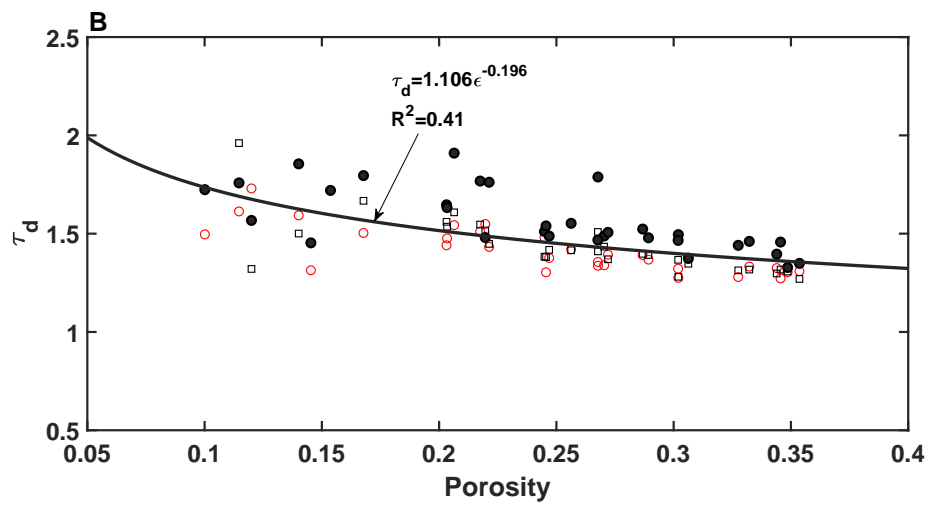
503

504 **Figure 2.** Comparison of tortuosity calculated from different methods. (A) The relationship
 505 between the geometrical tortuosity τ_g and the transport tortuosity calculated from solute
 506 diffusion τ_d (symbols), in comparison against the 1:1 line (solid line). (B) The relationship
 507 between the transport tortuosity and the **flow tortuosity** τ_f calculated from viscous fluid
 508 (symbols), in comparison against the 1 : 1 line (solid line).

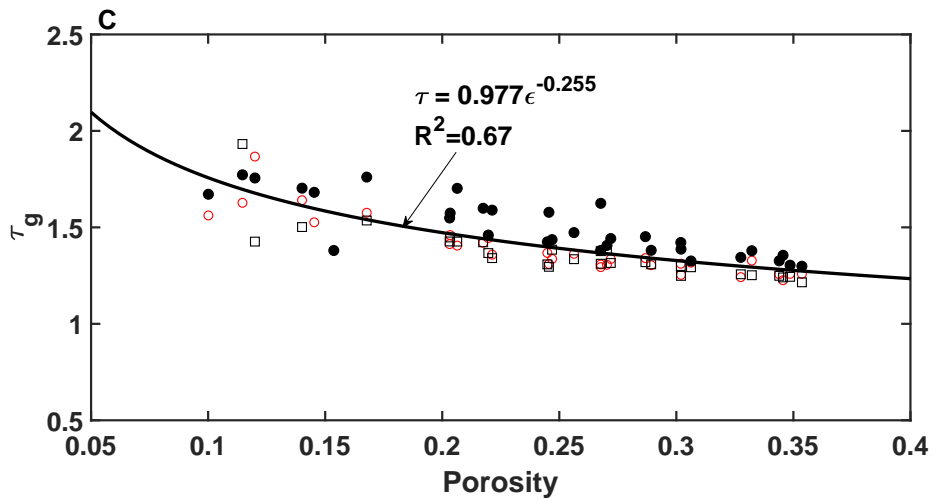
509



510



511



512

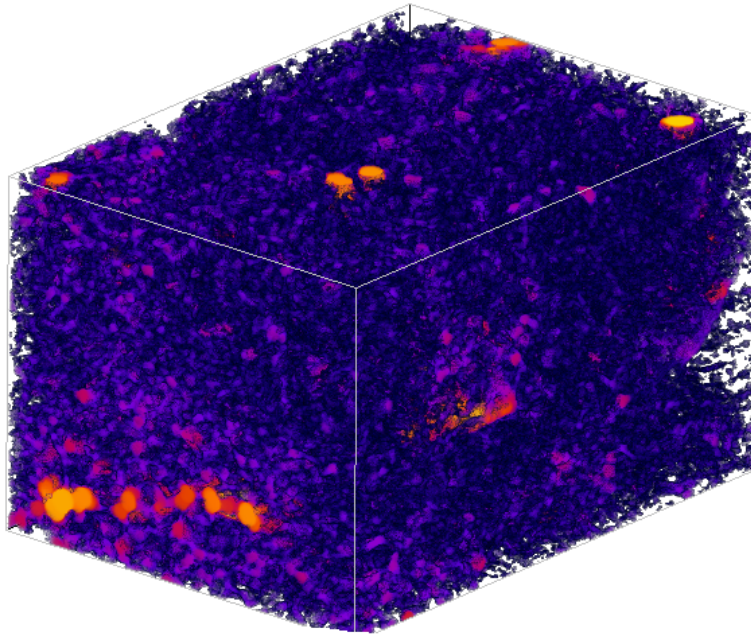
513 **Figure 3.** Change in tortuosity with porosity. (A) Flow tortuosity, (B) transport tortuosity, and
 514 (C) geometrical tortuosity.

515

516

517

518



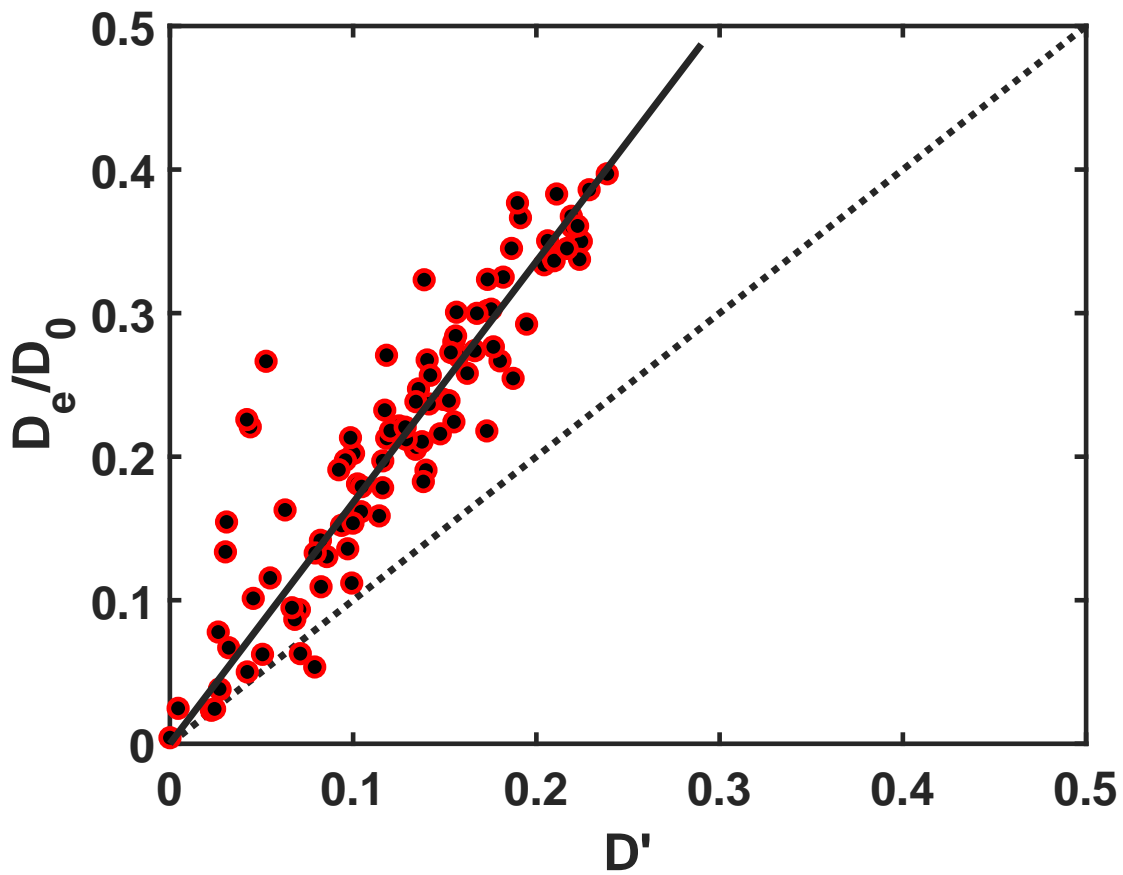
519

520

521 **Figure 4.** Spatial location of pores of different sizes calculated for Sample B in Figure 1
522 using the plugin Bone J in Image J. The pore size increases from dark to bright.

523

524



526

527 **Figure 5.** Comparison between the bulk diffusion coefficient calculated from the pore-scale
 528 simulations (normalised by its diffusion coefficient in water D_0) with that estimated from
 529 porosity and the geometrical tortuosity ($D' = \varepsilon/\tau_g^2$). The dotted line is the 1:1 line and the
 530 solid line is the fitting of $D_e/D_0 = 1.52D'$.

531